# Formation of amorphous Ti-50at.%Pt by solid state reactions during mechanical alloying

M.L. Mahlatji*†, S. Chikosha*, H.K. Chikwanda*, W.E. Stumpf†, and C.W. Siyasiya†
**CSIR/ MSM/LM*
*†University of Pretoria*

Mechanical alloying of an equiatomic mixture of crystalline elemental powders of Ti and Pt in a high-energy ball mill results in formation of an amorphous alloy by solid-state reactions. Mechanical alloying was carried out in an argon atmosphere at a rotation speed of 1200 r/min and a 20:1 ball-powder weight ratio for time intervals ranging from 4 to 40 hours. At an intermediate stage of mechanical alloying, scanning electron microscopy showed the formation of characteristic layered structures of inhomogeneous composition within the powder particles. X-ray diffraction analysis showed the gradual disappearance of crystalline Bragg peaks and at the same time the emergence of broad amorphous maxima as milling progressed. The amorphization process was completed after 8-12 hours. The amorphous state of the product indicated that temperatures during processing do not exceeded the crystallization temperature of the alloy.

***Keywords**:* TiPt alloy, mechanical alloying, amorphization, solid-state reactions.

## Introduction

Shape memory alloys (SMAs) undergo a reversible martensite transformation, which drives the thermoelastic properties of shape memory and pseudoelasticity (Otsuka and Ren, 1999). The Ti-50 at.%Pt alloy, which transforms from the high-temperature cubic B2 phase to the low-temperature orthorhombic B19 phase (Donkersloot and Van Vuch, 1970), has potential for high-temperature shape memory applications. The alloy has a reported martensite transformation temperature ($M_S$) of 1050°C (Biggs *et al*., 2001), and its pseudoelasticity and shape memory properties under stress-free conditions have been well documented (Yamabe-Mitarai *et al*., 2006, 2010). Shape memory applications in high-temperature environments such as in the aerospace, energy, and automotive industries require alloys with a high $M_S$ range (300-1000°C), much higher than the $M_S$ range reported for the commercially successful Ti-Ni alloys of just over 100°C (Otsuka and Ren, 2005). Although the addition of certain alloying elements can slightly raise the $M_S$ of Ti-Ni alloys (Firstov, Van Humbeeck, and Koval, 2004), higher transformation temperatures can be achieved only by high $M_S$ systems such as Ti-Pt. Alloying elements can then be used to reduce the $M_S$ according to specific applications and to improve ductility. Reduction of the $M_S$ also lowers the effect of diffusion-controlled processes such as recrystallization, recovery, and phase decomposition, which can be detrimental to the martensite transformation.

Conventional methods of forming the alloy typically involve plasma arc, electron beam, or vacuum induction melting, followed by a suitable thermomechanical treatment to homogenize and age the alloy. The present work explores mechanical alloying (MA) as an alternative means of producing the alloy. MA is a process of alloy formation from a mixture of powder particles in a high-energy ball mill (Soni, 2001). Chemical homogenization proceeds through a series of ball-powder-ball collisions (Figure 1), resulting in the repeated flattening, fracturing, and mutual cold welding of the powder particles coupled with short-range diffusion. This leads to the formation of a particulate alloy material suitable for consolidation and further processing.

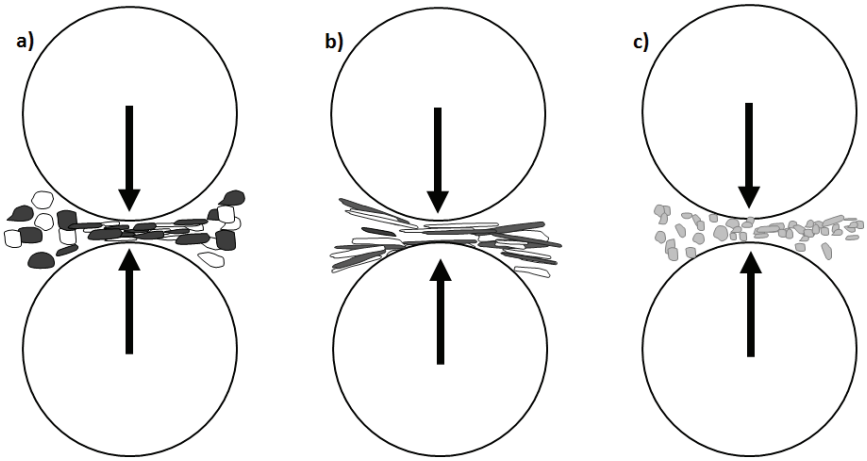


***Figure 1. Schematic of the different stages during MA of a nominally ductile powder mixture: (a) starting powder, (b) flattened, layered composite particles, (c) homogenous equiaxed particles***

MA of crystalline powder mixtures of two transition metals often results in the formation of amorphous alloys (Koch *et al.*, 1983; Schwarz and Koch, 1986). It is generally accepted that this is due to solid-state amorphization reactions (SSAR), driven by (a) a large negative heat of mixing in the amorphous state and (b) one element in the powder mixture having anomalously fast diffusivity in the other (Johnson, 1986). These conditions ensure the availability of a sufficient thermodynamic driving force for the amorphization reaction and that the amorphous phase forms at a reasonable rate, faster than the competing crystalline equilibrium phase(s). The free energy state of such a process can be generally illustrated by the schematic free energy diagram of Figure 2,where it is assumed that a fully homogenous amorphous alloy with composition X is formed from a starting crystalline powder mixture of A and B. The free energy of the amorphous phase, indicated by the thick solid line curve, is shown together with the (dashed) schematic free energies of the crystalline α-A(B) and β-B(A) solid solution phases and the equilibrium crystalline γ-intermetallic phase.

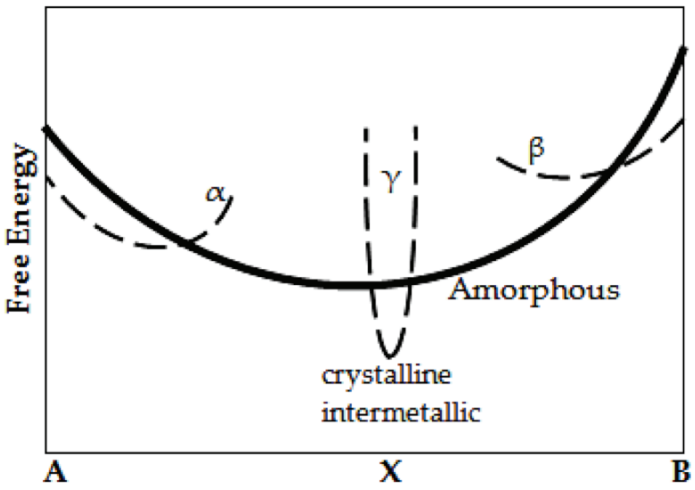


***Figure 2. Schematic free energy diagram showing the free energies of the amorphous phase, the crystalline solid solutions α and β, and the crystalline intermetallic γ phase***

The amorphous MA product formed by SSAR is a metastable phase that requires devitrification to form an equilibrium crystalline phase to be suitable for the envisaged shape memory applications. As Figure 2 suggests, such alloys typically have no thermodynamic barrier against crystallization of the amorphous phase, only a kinetic barrier which suppresses the long-range atomic diffusion required for crystallization (Johnson, 1986). The amorphous phase will therefore readily undergo crystallization when heated above its crystallization temperature ($T_x$), where enough activation energy becomes available to overcome the kinetic barrier against crystallization.

Compared to conventional melting methods, MA offers the advantages of solid-state processing and better composition control, with the possibility of directly forming near net shape parts that require minimum machining and metal loss to produce the final part dimensions. The disadvantages of MA include easy oxidation of powder particles due to the large activated surface area involved, and the formation of a nanocrystalline parent austenite phase, which has been shown to have a weakening effect on the martensite transformation (Waitz and Karnthaler, 2004; Guimaraes, 2007). It is generally accepted that this is due to the increasing difficulty in plastic accommodation in the austenite of shape strain of the martensite transformation with the reduction in grain size. This weakening effect has been demonstrated for Ti-Ni based SMAs formed by crystallization of an amorphous phase (Valeanu *et al*., 2011, Tian *et al*., 2009). The Ti-Pt system, however, has an $M_S$ that lies above the $T_x$ (477°C (De Reus and Saris, 1990)) of the alloy. For such alloys, the amorphous phase can be directly crystallized into the martensite phase with no prior austenite phase, as demonstrated for the Zr-Cu-Ni system (Firstov *et al*., 2006). The possibility of direct crystallization of B19-TiPt martensite from an amorphous phase therefore removes the limitations that would be associated with martensite formation from a nanocrystalline B2-austenite parent phase.

## Experimental methods

### *Mechanical alloying*

Elemental powders of commercially pure Ti and Pt were mixed in a 1:1 atomic ratio. The Ti particles were spherical and the Pt particles were spongy and irregular (Figure 3). MA was carried out in a Simoloyer CM01 ½ ℓ high-energy horizontal ball mill. The charge, composed of powder and milling balls, was loaded into the jar and the jar was sealed in an Ar-filled glove box. The MA parameters are shown in Table I. The jar was periodically discharged to control cold welding of powder to the milling equipment. The steady state external temperature of the jar never exceeded 37.8°C during MA due to cooling water running through the double-walled jar and flange connection. Externally cooling the jar helps transfer heat away from the contents and promotes particle fracture over ductile coating of walls, balls, and rotor.

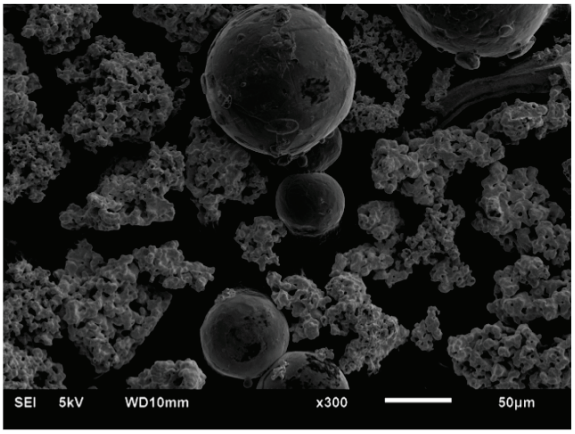


***Figure 3. SE-SEM micrograph of the starting powder for MA showing spherical particles (Ti) and spongy, irregular particles (Pt)***

Energy-dispersive X-ray (EDX) analysis showed increasing levels of contamination in the powder with increasing MA time. The major contaminants, identified as Fe, Cr, and Mo, corresponded with the hardened steel composition of the mill lining and rotor. Hence the contamination was attributed to wear of milling equipment. Fe levels in the milled powder ranged from ≤1.6 wt.%Fe after 4 hours to well over 20 wt.%Fe in powder milled for 16 hours and longer.

**Table I. Mechanical alloying parameters**

| | |
|---|---|
| Mill type | Simoloyer CM01 ½ ℓ |
| Ball-powder ratio | 20:1 (w/w); 100Cr6 Ø5mm milling balls |
| Milling intervals | 0, 4,8,12,16, 24, 32, 40 (h) |
| Milling atmosphere | Argon |
| Milling speed | 1200 (r/min), operating and discharging runs |

### *Structural characterization*

Phase characterization of the powder was performed using X-ray powder diffraction (XRD) in a Phillips PW 1710 powder diffractometer with Cu Kα radiation (λ = 1.5421 Å) over the 2θ range of 20-120°. Where applicable, the resulting diffraction patterns were analysed for average domain size and internal strain using the Scherrer method. Scanning electron microscopy (SEM) was carried out with a JEOL JSM-6510 microscope operating at 20 kV and equipped with an EDX detector. Transmission electron microscopy (TEM) work was performed with a JEOL JSM-2100 microscope operating at 200 kV with a beam current of approx. 112 $\mu$A.

## Results

### *Morphology of powder*

During the first few hours of MA, the powder displayed a strong tendency to cold weld to the balls and walls of the milling jar due to its ductility. The cold-welded powder was mostly restricted to a specific region of the jar and could be easily dislodged by turning the jar 180° at regular intervals and running a discharging procedure. While the formation of a thin coating on milling equipment can help prevent excessive wear and minimize powder contamination, the authors have previously observed that if the welded particles are not dislodged regularly to reintroduce the powder back into the MA process as free flowing powder, a heterogeneous final product will result. As MA progressed, plastic deformation strongly reduced the ductility of the powder particles until cold welding to the milling equipment was no longer observed. As Figure 5 shows for powder milled for 4 and 8 hours, the powder particles transform from a spherical/spongy morphology to a highly fissured morphology with a wide particle size distribution.

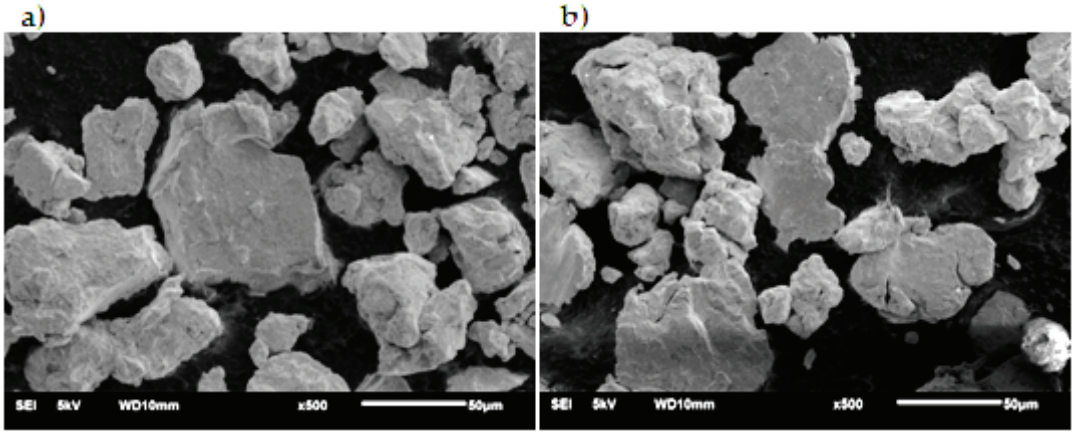


***Figure 4. SE-SEM micrographs of Ti-50at%Pt powder particles after MA for (a) 4 and (b) 8 hours***

SEM micrographs of sectioned particles at different stages of the alloying process after MA for 4 hours are shown in Figure 5. EDX analysis showed that the dark regions are pure Ti and the grey regions have a composition of 39 ≤ at.%Pt ≤51 while the bright regions have a Pt-rich composition. The repeated impact experienced by the powder particles when trapped between colliding balls plastically deforms and flattens them. Mutual cold welding of these flattened particles result in the lamellar structure of Figure 6(a). A similar layered structure at an intermediate stage of alloying of ductile metal powders was also reported by Benjamin and Volin (1974). The repeated fragmentation and cold welding of the powder particles refine the lamellar structure, resulting in a random orientation of the lamellae within the particles as seen in Figure 6(b). Continued structural refinement results in homogenization and disappearance of the layered structure, with the Pt-rich layers Figure 6(c) being the last to disappear. Beyond 4 hours of MA, all particles displayed a homogenous structure similar to Figure 6(d) with a near equiatomic composition.

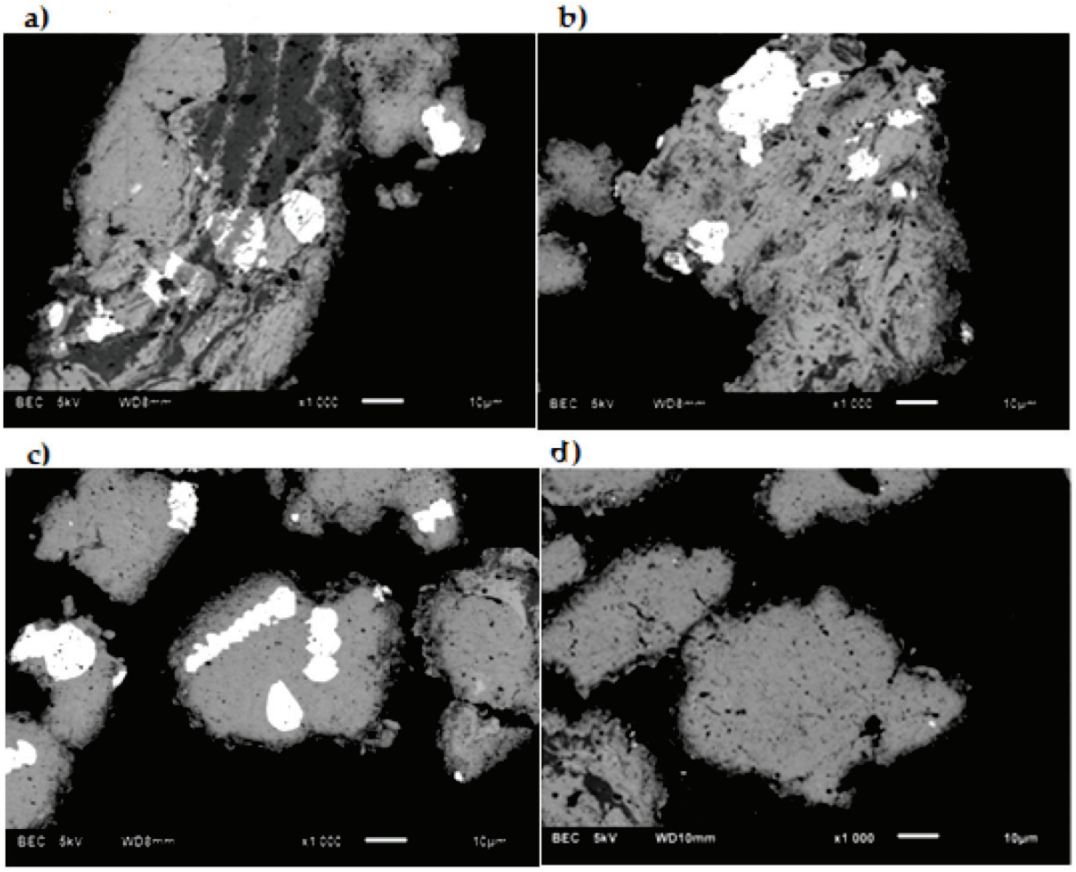


***Figure 5. Ti-50 at.%Pt cut and polished MA powder particles after 4 hours: (a) lamellar structure, (b) randomly oriented lamellae, (c) residual Pt-rich regions in homogenous matrix, (d) complete homogenization***

### *Crystallinity of powder*

Figure 7 shows a series of selected XRD patterns of Ti-50 at.%Pt powders at different MA time intervals. The pattern at 0 hours is a superposition of HCP Ti and FCC Pt reflection peaks, proving that the starting material was a mixture of elemental crystalline powders of Ti and Pt. After 4 hours, all Ti reflection peaks have disappeared and only broad low-intensity Pt reflections can be identified. At the same time, there is an emergence of the broad maxima characteristic of amorphous alloys. The residual nanocrystalline Ti in the composite layered particles of Figure 6(a-b) – Ti layer thickness ≤ 5 $\mu$m - is below the detection limit of XRD. Hence, no Ti reflections appear on the 4-hour scans.

The crystallite size of the powder was determined using the Scherrer method (Equation [1]), where $d$ is the average domain dimension along the scattering vector (Å), $K$ is a shape constant (=0.9), λ the wavelength ($K\alpha_{Cu}$ = λ = 1.5421 Å), θ the X-ray scattering angle, and β the line width (FWHM) after correction for instrument broadening with a Si standard. The tangent formula (Equation [2]) was used to determine the internal strain, where ε is the mean lattice distortion, and β and θ are as above. The average crystallite size (lattice strain) is reduced (increased) from 13 nm (0.87%) after 4 hours to 8.3 nm (1.30%) after 8 hours. For MA of 12 hours and beyond, all Bragg reflections have disappeared, indicating completion of the amorphization process.

$$d = \frac{K\lambda}{\beta \cos\theta} \qquad [1]$$

$$\varepsilon = \frac{\beta}{4\tan\theta} \qquad [2]$$

The accumulation of crystalline contaminants (mostly Fe) from wear of milling equipment, as detected by EDX, is not immediately apparent in the XRD patterns of Figure 6 due to the low resolution of XRD. The fully amorphous reflection after 12 hours, where the contamination level was still relatively low, has the major maximum centred near

the 2θ position corresponding to the strong FCC Pt (111) and HCP Ti (101) Bragg reflections as expected. The 32-hour pattern, however. shows how the major maximum has gradually shifted and is now centred at a higher 2θ position due to the accumulation of Fe-rich contaminants.

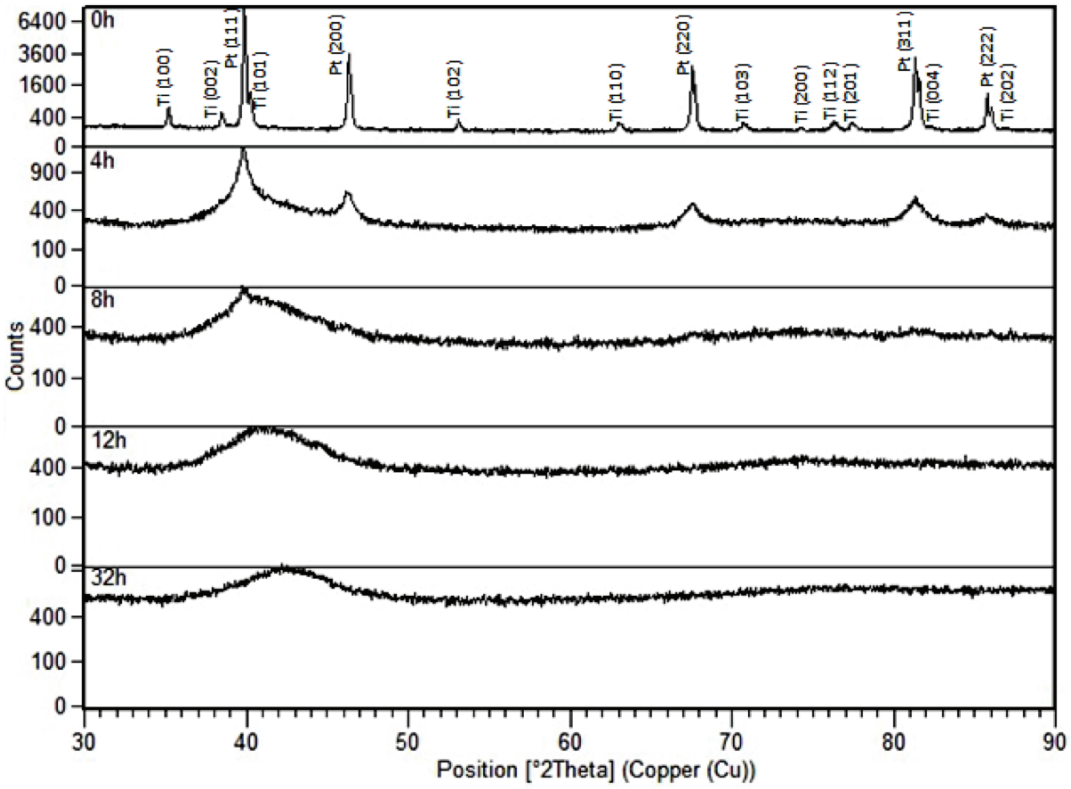


***Figure 6. X-ray diffraction patterns of Ti-50 at.%Pt at different MA time intervals***

The MA process was further studied by TEM for the time intervals corresponding to partial amorphization (4 hours' MA), fully amorphous alloy (12 hours' MA), and heavily contaminated amorphous alloy (32 hours' MA). Figure 8(a-b) shows TEM images with corresponding selected area diffraction (SAD) patterns after MA for 4 hours, where the amorphous phase coexists with un-reacted nanocrystalline Ti and Pt. This is reflected by the fine lattice fringes on the high magnification image and diffraction spots on the SAD. The lack of diffraction spots and lattice fringes on the powder after 12 hours (Figure 9a-b) proves that the powder is now fully amorphous, in agreement with the XRD results. After 32 hours (Figure 10a-b), SAD patterns show traces of crystalline diffraction spots in the amorphous matrix. The crystalline spots can be due to either (a) crystallization of the previously fully amorphous powder when the powder particles trapped between colliding balls experience a momentary temperature rise exceeding the $T_x$ of the alloy, or (b) the introduction of crystalline contaminant phases into the amorphous alloy. Temperature rise from ball impacts during MA has been estimated to be only a few hundred degrees (Joarder, Pabi, and Murty, 2004), well below the reported $T_x$ of amorphous Ti-50 at.%Pt alloy. The crystallites can therefore be attributed to contaminants from wear of milling equipment, as detected by the low-resolution analytical techniques. This indicates that MA should not be carried out for unnecessarily long time intervals, such as beyond the point of complete amorphization, to avoid contamination.

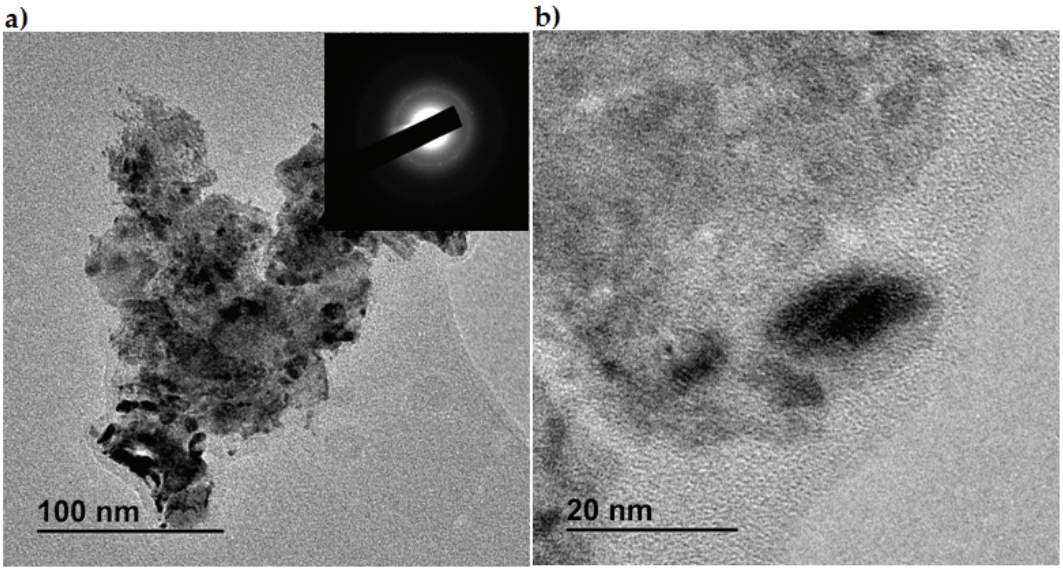


***Figure 7. Ti-50 at.%Pt powder after MA for 4 hours: (a) The SAD pattern shows an amorphous halo and crystalline diffraction spots, corresponding to the remaining crystalline phases, (b) lattice fringes in an amorphous matrix***

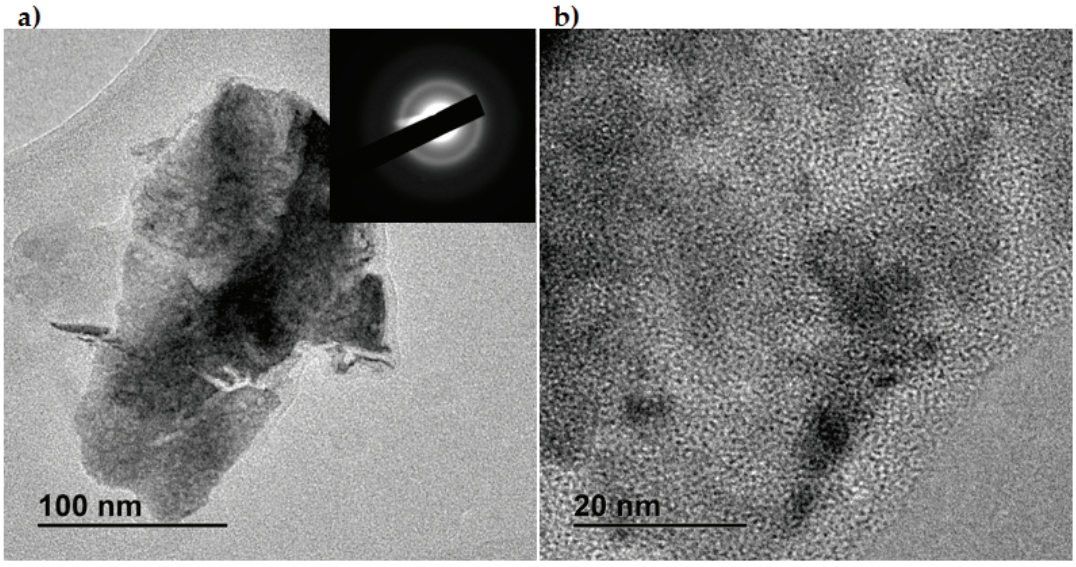


***Figure 8. Ti-50 at.%Pt powder after MA for 12 hours: (a) TEM image with corresponding SAD pattern showing the amorphous halo, (b) the amorphous phase***

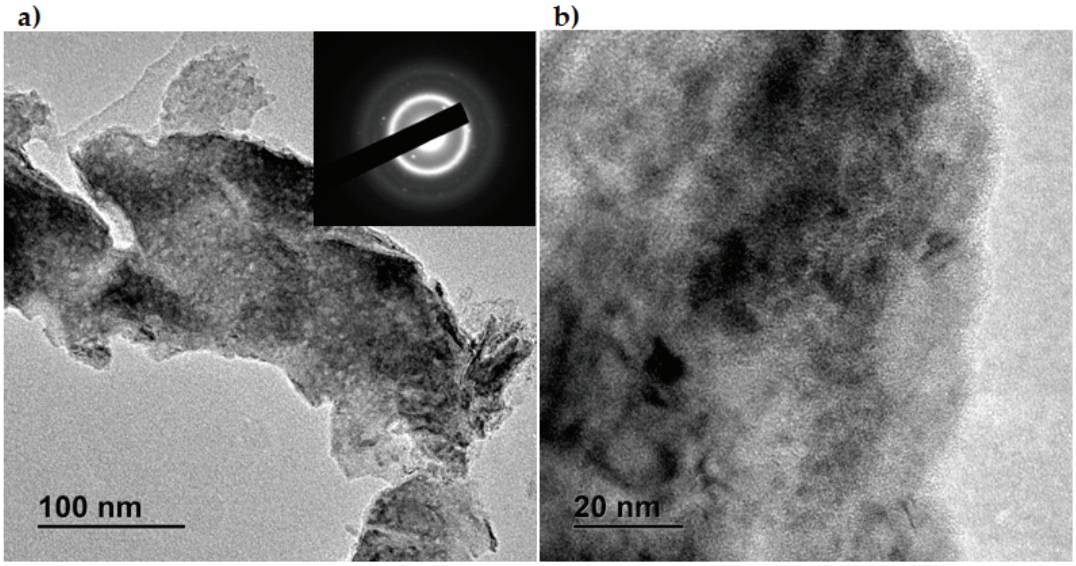


***Figure 9. Ti-50 at.%Pt powder after MA for 32 hours: (a) The SAD pattern shows the amorphous halo and crystalline diffraction spots, attributed to contamination from wear of milling equipment, (b) the amorphous phase***

**Discussion**

The formation of amorphous Ti-50 at.%Pt alloy is demonstrated through the transformation of Bragg elemental crystalline reflections of Ti and Pt at the start of MA into broad featureless reflections characteristic of amorphous alloys after MA for 8-12 hours. Similar results of amorphous phase formation by MA from elemental powder mixtures have been reported for the closely related TiNi (Schwarz, Petrich, and Saw, 1985; Liang, Wang, and Li, 1995) and TiPd (Thompson and Politis, 1987) systems. The deformation, fracturing, and cold welding of powder particles is illustrated by Figure 5(a-b), where the formerly spherical/-spongy particles have formed agglomerates, and in some cases have become flattened and fissured. These structural changes also result in a reduction in crystallite size and an increase in lattice strain. The characteristic layered structure shown in Figure 6(a-c), which precedes the appearance of the homogenous structure, indicates that the alloying process proceeds by SSAR. The layered structure is due to the preferential cold welding of newly created clean Ti and Pt boundaries formed by particle fracture. It has been suggested that conditions at the layer interfaces during an intermediate stage of MA of two metals closely resemble those within conventional thin-film diffusion couples (Johnson, 1988), leading to alloy formation by solid state interfacial interdiffusion reactions. According to the classification of Weeber and Bakker (1988), SSAR of two metals can proceed along three different paths, depending on the alloy system and experimental conditions. The XRD patterns of Figure 7 indicate that the Ti-Pt system undergoes a Type II reaction path, characterized by a decrement in intensity of the elemental crystalline reflections and separately an increment in intensity of the broad amorphous reflection.

The SSAR alloying mechanism observed in the current work is different from the observation made by (Maweja, Phasha, and Yamabe-Mitarai, 2012), where MA of Ti-50 at.%Pt powder in a high-energy ball resulted in formation of a disordered crystalline FCC Pt(Ti) extended solid solution. It is suggested that the different MA product phases are due to differences in milling parameters, such as the effect of using a process control agent (PCA) to control the cold welding of powder particles to milling equipment. A PCA was not used in the current work to avoid contamination and to optimize alloy formation. Besides improving the amount of free-flowing powder in the milling jar, PCAs have been shown to have a generally negative effect on the alloying process (Machio, Chikwanda, and Chikosha, 2011). Similar inconsistencies in the crystallinity of the milled product have also been observed in the MA of other alloy systems such as Ti-Ni, where formation of solid solutions and disordered intermetallics have been reported (Mousavi, Karimzadeh, and Abbasi, 2008; Takasaki, 1998) in addition to amorphous phase formation when using different MA parameters. Determination of the relative thermodynamic stability of the FCC Pt(Ti) solid solution, the amorphous phase, and the crystalline equilibrium phase under conditions of suppressed atomic diffusion (i.e., in the form of Figure 2) is required for a better understanding of phase transformations during MA of the Ti-Pt system.

While it is currently possible to measure the process temperature during operation of the high-energy ball mill only with a thermocouple attached externally to the wall of the milling jar, some general deductions can be made about thermal conditions inside the jar during operation. Two temperatures can be defined: (a) the ambient temperature in the jar and (b) the momentary temperature rise during high-speed ball collisions, which is expected to be much higher than

the ambient temperature. The amorphous phase is expected to readily crystallize into an equilibrium crystalline phase when heated above the $T_x$ of the alloy. The fully amorphous state of the milled powder after 8-12 hours proves that both the ambient and the ball-collision temperatures inside the milling jar do not exceed the $T_x$ of the alloy, otherwise the alloy powder would become crystalline.

## Conclusions

Amorphous Ti-50 at.%Pt alloy is formed by SSAR during MA of crystalline elemental powders of Ti and Pt. At an intermediate stage, the mechanical mixing and deformation leads to formation of characteristic layered particles. Amorphization is completed after 8-12 hours. Milling for longer time intervals beyond the completion of amorphization should be avoided as it results in powder contamination from wear of milling equipment. While it is currently possible to measure only the external temperature of the milling jar, it can be inferred from the amorphous state of the product that the temperature during processing does not exceed the $T_x$ of the alloy.

Analogies can be drawn between the formation of a homogenous amorphous alloy by MA and the formation of a homogenous molten alloy by ordinary melting. A liquid and an amorphous alloy with the same composition represent the molten and 'frozen' intermediate states in the process of forming crystalline alloys. The former requires cooling towards $T_x$ and the latter requires heating towards $T_x$ to form the equilibrium crystalline phase. An amorphous Ti-50 at.%Pt alloy formed by MA therefore represents a 'melt' phase, formed without heating above the excessively high melting points of the components and the corresponding intermetallic phase.

Future work includes devitrification of the amorphous alloy to form crystalline Ti-50 at.%Pt, suitable for shape memory testing. Semi-empirical thermodynamic modelling will be done to establish solid solubility limits of Ti in FCC Pt under polymorphous conditions, as well as the relative free energies of the solid solution, the amorphous and the crystalline α-TiPt phases at temperature below the $T_x$. This is required to understand the differences in the product phases formed during MA of the Ti-Pt system.

## Acknowledgements

The authors wish to thank the Department of Science and Technology and Anglo American Platinum for co-funding the work, and Anglo American Platinum for providing the Pt powder. The kind permission of both the CSIR and the University of Pretoria to publish this work is acknowledged.

## References

Benjamin, J.S. and Volin, T.E. 1974. The mechanism of mechanical alloying *Metallurgical Transactions*, vol. 5. p. 1929-1934.

Biggs, T. Cortie, M.B., Witcomb, M.J., and Cornish, L.A. 2001. *Metallurgical and Materials Transactions A*, vol. 32A. p. 1881.

De Reus, R. and Saris, F.W. 1990. *Materials Letters*, vol. 9. p. 487.

Donkersloot, H.C. and Van Vucht, J.H.N. 1970. *Journal of the Less-Common Metals*, vol. 20. p. 83.

Firstov, G.S., Koval, Y.N., Van Humbeeck, J., Portier, R., Ochin, P., and Vermaut, P. 2006. *Materials Science and Engineering A*, vol. 438-440. p. 816.

Firstov, G.S., Van Humbeeck, J., and Koval, Y.N. 2004. *Materials Science and Engineering*, vol. A378. p. 2.

Guimaraes, J.R.C. 2007. *Scripa Materialia*, vol. 57. p. 237.

Joarder, J.. Pabi, S.K,. and Murty, B.S. 2004. *Scripta Materialia*, vol. 50. p. 1199.

Johnson, W.L. 1986. *Progress in Materials Science*, vol. 30. p. 81.

Johnson, W.L. 1988. *Materials Science and Engineering*, vol. 97. p. 1.

Koch, C.C., Cavin, O.B., McKamey, C.G., and Scarbrough, J.O. 1983. Physics Letters, vol. 43. p. 1017.

Liang, G.X., Wang, E.D., and Li, Z.M. 1995. *Materials Science and Technology*, vol. 11. p. 347.

Machio, C., Chikwanda, H.K,. and Chikosha, S. 2011. *Journal of the Southern African Institute of Mining and Metallurgy*, vol. 111. p. 149.

Maweja, K., Phasha, M.J., and Yamabe-Mitarai, Y. 2012. *Journal of Alloys and Compounds*, vol. 523. p. 167.

Mousavi, T., Karimzadeh, F., and Abbasi, M.H. 2008. *Materials Science and Engineering A*, vol. 487. p. 46.

Otsuka, K. and Ren, X. 1999. Recent developments in the research of shape memory alloys. *Intermetallics*, vol. 7. pp. 511-528.

Otsuka, K. and Ren, X. 2005. *Progress in Materials Science*, vol. 50. p. 511.

Schwarz, R.B. and Koch, C.C. 1986. *Applied Physics Letters*, vol. 49. p. 146.

Schwarz, R.B., Petrich, R.R., and Saw, C.K. 1985. *Journal of Non-Crystalline Solids*, vol. 76. p. 281.

Soni, P.R. 2001. Mechanical Alloying: Fundamentals and Applications. Cambridge International Science Publishing, Cambridge, UK.

Takasaki, A. 1998. *Physica Status Solidi A*, vol. 169. p. 183.

Thompson, J.R. and Politis, C. 1987. *Europhysics Letters*, vol. 3. p. 199.

Tian, B., Tong, Y.X., Chen, F,. Liu, Y., and Zheng, Y.F. 2009. *Journal of Alloys and Compounds*, vol. 477. p. 576.

Valeanu, M., Lucaci, M., Crisan, A.D., Sofronie, M., Leonat, L., and Kuncser, V. 2011. *Journal of Alloys and Compounds*, vol. 509. p. 4495.

Waitz, T. and Karnthaler, H.P. 2004. *Acta Materialia*, vol. 52. p. 5461.

Weeber, A.W. and Bakker, H. 1988. *Physica B*, vol. 153. p. 93.

Yamabe-Mitarai, Y., Hara, T., Miura, S,. and Hosoda, H. 2006. *Materials Transactions*, vol. 47. p. 650.

Yamabe-Mitarai, Y., Hara, T., Miura, S., and Hosoda, H. 2010. *Intermetallics*, vol. 18. p. 2275.

**The Author**

**Malesela Linda Mahlatji,** *Candidate Researcher*, CSIR

The presenter completed her BEng degree in Metallurgy at the University of Pretoria in 2010 and completed the Honours degree in 2011. Since 2011 the presenter has been part of the Powder Metallurgy Technologies research group at the CSIR with a research focus on Ti-Pt high temperature shape memory alloys.